Classification: Biophysics and Computational Biology

Evidence for formation of DNA repair centers and dose-response non-linearity in human cells

Teresa Neumaier[1], Joel Swenson[4,5], Christopher Pham[3], Aris Polyzos[3], Alvin Lo[3], PoAn B. Yang[3], Jane E. Dyball[3], Aroumougame Asaithamby[2], David J. Chen[2], Mina Bissell[3], Stefan Thalhammer[1], Sylvain V. Costes[3,*]

1. Institute for Radiation Protection, Helmholtz Zentrum München, German Research Center for Environmental Health (GmbH), Ingolstädter Landstraße 1, 85764 Neuherberg, Germany
2. Division of Molecular Radiation Biology, Department of Radiation Oncology, University of Texas Southwestern Medical Center at Dallas, Dallas, TX 75390, USA
3. Department of Cancer and DNA Damage Response, Lawrence Berkeley National Laboratory, 1 Cyclotron Road, MS977, Berkeley CA 94720, USA
4. Department of Molecular and Cell Biology, University of California, Berkeley.
5. Department of Genome Dynamics, Lawrence Berkeley National Laboratory, 1 Cyclotron Road, MS977, Berkeley CA 94720, USA

* Corresponding author
Sylvain V. Costes
Department of Cancer and DNA Damage Response, Lawrence Berkeley National Laboratory, 1 Cyclotron Road, MS:977, Berkeley CA 94720, USA
Phone: 001- 510-486-6988
FAX: 001-510-486-5625
Email: svcostes@lbl.gov

Abstract

The concept of DNA 'repair centers' and the meaning of radiation-induced foci (RIF) in human cells have remained controversial. RIFs are characterized by the local recruitment of DNA damage sensing proteins such as p53 binding protein (53BP1). Here we provide strong evidence for the existence of 'repair centers'. We used live imaging and mathematical fitting of RIF kinetics to show that RIF induction rate increases with increasing radiation dose, whereas the rate at which RIFs disappear decreases. We show that multiple DNA double strand breaks (DSB) 1 to 2 μm apart can rapidly cluster into repair centers. Correcting mathematically for the dose dependence of induction/resolution rates, we observe an absolute RIF yield that is surprisingly much smaller at higher doses: 15 RIF/Gy after 2 Gy exposure compared to ~64 RIF/Gy, after 0.1 Gy. Cumulative RIF counts from time lapse of 53BP1-GFP in human breast cells confirmed these results.

The standard model currently in use applies a linear scale, extrapolating cancer risk from high doses to low doses of ionizing radiation. However, our discovery of DSB clustering over such large distances cast considerable doubts on the general assumption that risk to ionizing radiation is proportional to dose, and instead provide a mechanism that could more accurately address risk dose dependency of ionizing radiation.

\body

Introduction

DNA damage sensing proteins localize at sites of DNA double strand breaks (DSB) within seconds to minutes following ionizing radiation (IR) exposure, resulting in the formation of immunofluorescently stainable nuclear domains referred to as radiation-induced foci (RIF) (1-3). RIF numbers are routinely used to assess the amount of DNA damage and repair kinetics after different treatments (4). However, there is a controversy surrounding the question of whether there is a 1:1 correspondence between RIFs and DSBs. For example, pulse field gel electrophoresis (PFGE) analysis suggests that DSBs decay exponentially with time directly after exposure (5)). In contrast, DNA damage sensing proteins do not instantaneously detect DSBs, leading to delayed kinetics for both detection and resolution. More specifically, the maximum number of 53BP1 or γH2AX RIFs is not reached until 15 to 30 min after exposure, and the yield of DSBs predicted by RIFs is typically lower than the expected 25-40 DSB/Gy measured by PFGE (4).

Dose response provides another assay for assessing the relationship between DSBs and RIF. Based on theoretical Monte Carlo simulations and PFGE measurements (6, 7), the frequency of DSBs should be highly correlated with radiation dose. Confirming this prediction, two research groups reported that RIF number is proportional to radiation dosage from 1 mGy to 2 Gy (8, 9). In both studies, methods were applied to identify "real" RIF at low doses, where frequencies may be close to background levels before IR (e.g.10 mGy would lead to about 0.3 DSB/cell). They either used cells with very low γH2AX background foci (*i.e.* 0.05 background foci/cell in primary human lung MRC-5 fibroblasts) (8), or performed live studies with a tagged DNA damage marker (*i.e.* 53BP1-GFP) and disregarded foci that were present before exposure to IR (9). However, there were discrepancies between these two studies. One study reported a 1:1 correspondence between RIF and DSBs, with a maximum of 35 γH2AX RIF/Gy at 3 min post-IR exposure (8), whereas the other study reported RIF frequencies were maximal much later (*i.e.* 30 to 60 min post-IR), with different proportionality: i.e. 16-20 53BP1-GFP RIF/Gy for human HT1080 and 60 53BP1-GFP RIF/Gy for immortalized human bronchial epithelial cells (9). These discrepancies cast some doubts on the one to one correspondence between RIF and DSB and also show that cell type and methods of analysis play both a crucial role in RIF quantification. Furthermore, dose/response linearity is not always observed. For example, in normal human fibroblasts (1) and in hamster V79 cells (10), we observed a maximum of 18-24 γH2AX RIF/Gy after exposure to less than 1 Gy of X-rays, compared to 13-15 γH2AX RIF/Gy for 1-4 Gy. Similarly, human fibroblasts showed a slight decrease with averages going from 21 to 17 RIF/Gy between 0.05 and 0.25 Gy, which was consistent across 18 independent lines (11).

Most studies measure RIF only at discrete times after the induction of damage. This means that the temporal complexity of the biochemical response, primarily initiated by DNA damage, is often neglected. However, temporal delays in RIF formation relative to DSBs as well as different resolution times for RIF complicate the interpretation of RIF numbers. In addition, even when kinetic studies are performed, the number of RIF reported at any given time after IR can never reflect the total number of RIF that have been produced by IR, as all RIFs that have already been resolved or that have not yet been produced are not counted.

Here we present a mathematical formalism that extracts the absolute number of RIF from RIF kinetics data. By integrating this biophysical model with a standardized high-content imaging methodology, we demonstrate the ability to get reproducible RIF results from different research laboratories. Since visual scoring of relatively small numbers of nuclei adds both statistical uncertainty (8) and subjective bias, we also developed true 3D automatic focus detection software, refined from previous versions (2), to allow scoring in a high throughput context. Miniaturization of cell cultures, using microwell slide technology, were also applied to further accelerate and normalize sample treatment and processing. All kinetic rates and RIF yield were confirmed using live studies of non-malignant human breast cells transfected with 53BP1-GFP. This comprehensive quantitative analysis challenges the concept of linearity between IR dose and RIF yield and suggest the existence of DNA repair center in human cells.

Results

Validation of RIF yield and formation-disappearance kinetics models using live cells exposed to X-rays

We proposed a mathematical model to fit the kinetics of RIF formation, which can deduce the absolute number of RIF produced by a given dose of ionizing radiation from the net number of RIF measured at any time point (see Material and Methods, above). Live cell imaging is ideal to validate such a model, because it simultaneously measures the number of RIF at any given time and the number of RIF accumulated since the time of exposure to Xrays. To test the validity of our model, we fitted with equation 1 the number of RIF measured in MCF10A transiently transfected with 53BP1-GFP. Both the number of RIF counted at each time frame, as well as the cumulative number of RIF counted after IR exposure, were scored (representative snapshots and kinetics are shown in Fig. 1A and 2A for 0.1 and 1 Gy respectively). If equations 1 and 2 were correct, the cumulative RIF counts (red curves shown in Fig. 1B and 2B) should converge over time to a constant value equal to the total number of RIF/Gy (α).

Confirming this biophysical model, fits of the net kinetics (green curves in Fig.1B and 2B) with equation 1 led to an α value that matched the total cumulated yield. In addition, live cell imaging revealed that the total number of RIF produced by IR was not proportional to dose, and was relatively lower at higher doses (73 RIF/Gy vs 28 RIF/Gy at 0.1 and 1 Gy respectively). In addition, RIF induced by low doses appeared more slowly and were resolved faster than after 1 Gy, as indicated by the reported formation and resolution half-lives on the graph ($T_{1/2}$). This led to a larger differential between the maximum number of RIF measured at any time point and the total cumulative number of RIF at low dose (indicated by arrows on graphs). 3D time lapse using confocal microscopy on human fibrosarcoma HT1080 stably transfected with 53BP1-GFP, showed very similar properties for 0.05, 0.1 and 1 Gy (Fig. S1). Finally, monitoring the intensity profiles of individual RIF during time lapse imaging identified changes in RIF size and intensity during focus formation (blue dashed rectangle in Fig. 1A and 2A). The relative intensity profiles for individual foci (1D intensity cross section of focus location normalized to the average 53BP1 intensity outside foci regions) and their averages are shown in Figs. 1C and 2C. Even though no difference in size could be observed, with an average RIF diameter of 0.64 μm for both high and low dose, a three fold increase of RIF intensity was measured after high dose.

High-content analysis on fixed specimens confirm non linear RIF yield with dose

In order to quantify a larger dataset representing endogenous levels of proteins, we analyzed arrays of fixed MCF10A by immunostaining for 53BP1. As described in material and methods, detection of RIF was done automatically, using improved in-house RIF detection algorithms (2). The computer scoring obtained in this manner was corroborated for a subset of cells counted manually at 30 min after different doses of X-ray (from 0.05 to 2 Gy - Fig. S2). Fig. 3A-C show representative images for selected doses, showing the efficiency of the algorithm for separating touching foci. Applying this approach for fitting average counts of 7 independent experiments measured at various doses of X-rays collected over a 24-hour time course, we observed excellent agreement with equation 1 (Fig. 3D). All fitted coefficients for equation 1 are summarized in Table 1. Similarly to what we observed with 3D time lapse, the absolute number of 53BP1 RIF normalized to dose (α in RIF/Gy/nucleus) decreased approximately 4 fold between 0.1 and 2 Gy (~64 ± 6 to 16 ± 2 RIF/Gy, after 0.1 and 2 Gy respectively). This decreasing trend was statistically significant (P-value < 0.01 using T-test). RIF kinetics were also dose dependent: RIF formation was twice as fast and RIF resolution was ~5 times slower at 2 Gy versus 0.1 Gy. Both k_1 and k_2 dose dependence were significant (P-value < 0.05 using one way ANOVA). To test if the dose-dependent DNA damage response was specific to breast epithelial cells, the same measurements were made on immortalized human skin fibroblasts (HCA2) grown as confluent populations (1), where we observed a similar trend, with a 1.7 fold decrease of RIF yield α, a 2.5 fold increase in 53BP1 RIF induction rate and a 20 fold decrease in RIF resolution rate between 0.1 and 2 Gy (Fig. S3).

To test the validity of the mathematical model further, we perturbed the rates of RIF formation or RIF removal by inhibiting ATM activity with KU55933 (see Material and Method). ATM inhibition was confirmed by measuring the reduction of phosphorylated P53 at S15 (Fig. 3E). As expected, the overall number of RIF was largely diminished (Fig. 3F). However, the same behaviour was observed: i.e. RIF yield dropped by 2 fold between 0.1 and 2 Gy (25±17 vs. 12±2 RIF/Gy). Fitted parameters are shown in Figs. 4A-C. Interestingly, detection half-lives were comparable with or without ATM inhibition across all doses, whereas resolution was significantly slower at high doses when ATM was inhibited (significant difference between 15.4±1.8 hrs with inhibition and 5.7±1.6 hrs without inhibition, after 2 Gy). This indicates that DSBs requiring longer repair time are still being detected at the same rate, in the absence of ATM.

RIF analysis in human cells exposed to densely ionizing radiation reveals self-exclusion of near-by RIF

In order to further explore the saturation effect of RIF numbers observed at higher dose, one would need to look at the DNA damage response for doses of X-rays higher than 2 Gy. However at such high doses there are several confounding factors: 1) there is the difficulty of resolving high numbers of RIF in the nucleus and, 2) the physiological effects on the cells manifest at higher doses (e.g. toxicity, cell cycle arrest, etc.). In order to circumvent these issues, we used high energy Fe ions (1 GeV/amu), referred to as HZE (High Z and energy). As illustrated in Fig. S4, HZE particles typically deposit part of their energy along linear tracks referred to as cores, and the other part is deposited from electrons randomly outside the core (i.e. Delta-rays) scattered by Coulombic interaction with the particles. The radius of the core is about ~10 nm for 1 GeV/amu Fe ions whereas Delta-rays radiate ~270 μm from the track (17, 18). As we described previoulsy (2), we have developed imaging tools that automatically identify these

tracks and can discriminate RIF along the tracks from random RIF in the nucleus (presumably generated by Delta-rays – Fig. S4). In order to account for RIF and physiological chromatin movement over time, all RIF detected within a 0.5 μm radial distance from the particle trajectory were considered 'core RIF'. Assuming a radial dose distribution decreasing as the distance square (19, 20), we estimated a dose of 26 Gy within the 0.5 μm radius track, and 0.17 Gy from Delta-rays dispersed outside that region (Fig. S4). Thus, HZE particle radiation allowed us to compare two compartmentally distinct radiation doses within the same cell (representative images shown in Fig. 4AB). We noted that core RIF sizes and intensities (Fig. 4C) were comparable to 1 Gy X-ray foci (Fig. 2C) as early as 1.5 min post-IR. However, core RIF were larger and brighter by 30 min post-IR. In contrast, delta-rays RIF size and intensity kinetic was comparable to X-rays (Fig. 4C vs Fig. 1C respectively).

In addition, our results confirmed what was observed for X-rays: i.e. high local doses along the track led to much faster RIF induction (~5 sec) and slower RIF resolution (~10 hours half-lives) than in the low dose region of the Delta-rays (2.8 min and 3.3 hours, respectively). The fitted coefficients are plotted against all other conditions studied in this work in Fig. 5A-C and listed in Table 1. Note that the measured RIF yield along the tracks was fitted to be 0.83 RIF/μm but could not be plotted against other α values in Fig. 5A since it was in a different unit.

Similar differences in RIF kinetics between track RIF and Delta-ray RIF were also observed in live cell imaging of MCF10A cells transiently transfected with 53BP1-GFP (Fig. S5). Time lapse imaging showed that after initial foci formation there were few new foci appearing along the tracks, whereas new Delta-ray RIF outside the track kept appearing during the initial 30 min post-IR period. Similar results were observed also in stably transfected human bronchial epithelial cells (HBEC) exposed to 1 GeV/amu O ions (Fig. S6).

Discussion

Single time or single dose measurements are snapshots and might not capture the complexity of the IR response of DNA damage-sensing proteins. Here we present a methodology and a mathematical kinetic model that can characterize the DNA damage response simultaneously across both time and dose levels. Our results provide a more accurate model of RIF dose response, and underscore fundamental concerns about static image data analysis in the dynamic environment of the living cell. We observe that as the number of DSB increases in a cell, the number of RIF does not increase proportionally and the kinetics of RIF formation/disappearance is altered; RIF appear faster but remain longer in the cells as dose levels increase. These non-linear processes cast considerable doubts on the general assumption that risk to ionizing radiation is proportional to dose and could be interpreted as the consequence of DNA repair centers in human cells.

Clustering of DSB into repair centers at high dose

As recently reviewed (4), most studies in the literature report RIF yield well below the expected 25-40 DSB/Gy measured by PFGE in cells in the G1 part of the cell cycle (5, 8). This probably reflects the fact that what is measured at any time-point is the net number of RIF that have formed since radiation, which does not account for RIF that have already been resolved, or for RIF that have not yet appeared. The time lapse imaging presented here shows clearly that RIF

formation continues to occur well beyond initial IR exposure time. In addition, our biophysical model fit well the kinetics curves observed for the number of RIF per nucleus and account for these missing RIF. These fits suggest that the absolute RIF yield normalized to dose (α), is not constant but drops 4 fold between 0.1 Gy and 2 Gy. The lower yield of α at high dose cannot be explained by depletion of the pool of 53BP1. Indeed, protein depletion would only lead to dimmer foci, not fewer foci. Furthermore, RIF number saturation cannot be due to overlapping foci since the expected spatial random distribution of DSBs simulated by computer (see Material and Methods) predicts average distances easily resolvable by light microscopy at the highest dose considered (2 Gy). Similarly, using radiation that deposits a high amount of energy along a tightly defined track, we observe ~0.7-0.8 RIF/µm along 1 GeV/amu Fe (Linear Energy Transfer, LET= 150 keV/µm), contrary to a theoretical value based on physical considerations of ~1.1 DSB/µm (2). In addition, when cells are exposed to ions with a hundred times higher energy densities (e.g. Uranium ions with LET of 14,300 keV/µm and expected ~100 DSB/µm), RIF frequencies remain in the same order of magnitude (*i.e.* 0.96 XRCC1 RIF/µm) (21), suggesting full saturation of the number of RIF. One potential explanation for this apparent saturation is the existence of repair centers with a minimum inter-distance of approximately 1 µm. If repair centers exist, as the local dose increases, the probability of having two DSBs migrating into one common RIF increases, leading to lower RIF counts per dose, faster induction and slower resolution.

Note that a distance of 1-2 µm is in good agreement with previous estimate of the distance between two separate DSBs which can explain DSB mis-rejoining data leading to the classic supra linear dose-dependence observed for radiation-induced chromosomal rearrangements (22, 23). Time lapse imaging also suggests that if DSB clustering takes place, it happens before a RIF is formed, since RIF clustering was not observed within the first 30 min post-IR. On the other hand, we did observe the merging of RIF over hours post-IR. RIF merging over long time course has already been described along high energy density tracks (24), and has been interpreted as transient clusters that eventually separate again (25).

In this work, we hypothesize that DSBs clustering occur rapidly after IR and that RIF formation reflects the repair machinery put in place around one DSB cluster. DSB clustering can then be rewritten as follow: $\beta \times DSB \xrightarrow{k_1} RIF \xrightarrow{k_2} RIF_{resolved}$ where $\beta(D)$ is the average number of DSB within one RIF. Assuming 35 DSB/Gy, $\beta=35/\alpha$ and based on our data, it increases with dose: β~1 DSB/RIF at 0.4 Gy suggesting a 1 to 1 correspondence, whereas there would be β~2.3 DSB/RIF after 2 Gy. Resolving these equations would then show that the real induction rate for RIF is in fact $k_1'=\beta.k_1$, where k_1 is dose independent and only reflects the time it takes to detect one DSB. The increasing induction rate with doses would then simply reflect β increasing with dose. Our data also show that RIF intensity is larger for higher doses while RIF sizes are similar. This suggests the existence of a well defined chromatin scaffold for these repair centers, with the presence of multiple DSB requiring more 53BP1 proteins compacted within the same structure. Note however that the rigidity of these repair centers is not absolute; this is because we noticed that RIF are both brighter and larger for extremely high doses along HZE tracks.

DNA damage repair centers have been clearly established in *Saccharomyces cerevisiae* (26) but they remain hypothetical in mammalian cells, as initially suggested by Savage (27, 28). However,

there are some data suggesting their existence in human cells. For example, there were indications in human blood cells that chromosomal rearrangements observed after exposure to densely ionizing radiation could be explained by localized movement of chromatin containing damaged DNA into local repair centers (29). Following up on this work, it was more recently shown that increasing LET of an α particle did not increase the total number of aberrations per track traversal, and instead increased the ratio of complex to total aberrations (30). Therefore, if DSB clustering occur, as LET goes up (for LET>100 keV/μm), RIF linear frequencies would not change significantly but each RIF would be made of more DSBs, increasing the probability of complex chromosomal rearrangements. In agreement with this theoretical argument, high resolution imaging of high-LET tracks in combination with Monte Carlo simulation have suggested recently the presence of multiple DSB within one single RIF (31). Similarly, a recent theoretical follow-up study taking into account the track structure of high energy ions and the supercoiled topography of DNA, confirmed that multiple DSB can be contained within one single RIF (32). Finally, we previously showed that spatial RIF distribution along high LET tracks implied relocalization of DSBs rapidly post-IR (2) and an independent study reached the same conclusion as 53BP1 RIF pattern along tracks differed significantly from theoretical expectations assuming a simple model of homogenous chromatin distribution (33). Whereas our data brings additional evidence of the existence of repair centers in human cells, the mechanisms by which such clustering take place remain entirely unknown at this point: are DSB clusters the result of random coalescence induced by DNA damage binding complexes (24) or is there an active transport of DSB towards pre-existing repair centers?

RIF resolution kinetics reflect both break complexity and break density

If we were to accept the classic definition that a complex DSB is made by at least 3 single strand breaks (SSB) within 10 base-pairs (34), then it is estimated that 20 to 30% of DSB are complex after exposure to low-LET radiations. In contrast, 70% of the damage induced by the ion used in this work (1 GeV/amu Fe) is complex (35). The resolution kinetics constants reported here show large difference of resolution kinetics between these two radiation qualities, with half-lives for RIF resolution as fast as 1.4 hours after 0.1 Gy of X-rays and as slow as 10 hours after high-LET for an estimated local dose of 26 Gy along Fe ions tracks. In comparison, using pulse field gel electrophoresis or neutral filter-elution using much higher doses of X-ray (>10 Gy), the fast repair half-life associated with simple DSB is ~5-30 min and the slow repair half-life is ~4-10 hours half-life (15, 16). Therefore, even though RIF resolution does not only reflect DSB repair, but delays due to the clearing of 53BP1 after repair, as suggested by other studies (36, 37), IR-induced DSB repair kinetics correlate well with RIF disappearance. Classically, the different DSB repair kinetics between different LET has been interpreted as additional delays for repairing complex DSBs. However, our work suggests that using the same LET, local dose effects alone can affect resolution kinetics: there is a 4 fold increase in RIF resolution half lives between 0.1 Gy and 2 Gy of X-rays (5.7 hours at 2 Gy). Therefore we conclude that slower DSB repair kinetic may not only reflect the presence of complex breaks, but also the presence of multiple DSB within one repair center, leading to a repair machinery having difficulty handling multiple ends of DNA strands in the same location.

High RIF yield at low dose for MCF10A

Under normal conditions, we detect many more RIF than expected in MCF10A after 0.1 Gy (64 RIF/Gy detected vs 35 RIF/Gy expected), especially in live cell imaging (73 RIF/Gy). Note that this leads to β value less than 1. This effect seems to be cell dependent: similar but more modest yields were observed for live imaging of fibrosarcoma cells HT1080 with 49 RIF/Gy and 40 RIF/Gy following 0.05 Gy and 0.1 Gy, respectively; and 30 RIF/Gy following 0.1 Gy in fixed normal human skin HCA2. In addition, we have not confirmed that the increase of RIF yield at low dose correlates with other surrogate markers of DNA damage such as chromosomal aberrations or micronuclei.

We also show here that ATM inhibition result in 3 fold reduction of α after 0.1Gy of X-rays with a yield of 25 RIF/Gy whereas no significant reduction of α is observed after 2 Gy with a yield of 12 RIF/Gy comparable to 15 RIF/Gy under normal conditions. This suggests that the higher RIF yield at low dose IR is ATM dependent. Since ionizing radiation can induce heterochromatin decondensation in Drosophila cells (40) or in mammalian cells (41), one could thus hypothesize that low doses of ionizing radiation induce a global but subtle chromatin reorganization which could lead to increase foci that may not necessarily relate to more DNA damage. In agreement with this hypothesis, ATM has been shown to autophosphorylate and consequently phosphorylate H2AX when nuclear volumes are dilated by using hypotonic media (38). Similarly it has been shown that hypotonic conditions alone are sufficient to induce binding of 53BP1 to chromatin (39).

Impact of results for regulating risk of ionizing radiation on human populations

The current literature has assumed the linear-no-threshold hypothesis (LNT), which implies that any amounts of ionizing radiation (IR) are harmful. LNT is used to set dose limits for radiation occupational workers or the general public. The LNT is based mainly on data from the Japanese A-bomb survivors and secondarily on arguments involving the dose-response of surrogate endpoints. Gene mutations are thought to be the initiating events of cancer and they can occur via misrejoining of two DNA double strand breaks (DSB) or via point mutation. Physical laws lead us to believe DSB frequencies are proportional to dose. Therefore, it is well accepted that point mutations are linear with dose since it requires only one DSB, whereas DSB misrejoinings are dependent to the dose squared (42). In the dose-range of radiation cancer epidemiology, the quadratic term is almost always negligible, especially at low dose rates, as the first lesion is probably repaired before the second mutation occurs (43). However, DSB clustering at 1 Gy and above may increase the quadratic term leading to higher number of DSB misrejoining at these doses. Therefore, extrapolating risk linearly from high dose as done with the LNT could lead to overestimate of cancer risk at low doses.

Materials and Methods

Cell culture

Cell culture of non-malignant human mammary epithelial cells (MCF10A, purchased from ATCC) were grown on 8-well Lab-Tek chambered coverglass (Nalge Nunc International,NY) or on 48-spot functionalized glass slides (AmpliGrid, Beckman Coulter GmbH, Krefeld, Germany). The cells were cultivated (in either 100 or 5 µl volumes, respectively) until they formed a

monolayer (~85% confluent) prior to irradiation. See SI Materials and Methods and Fig. S7 for full details.

Irradiation and ATM inhibition

The cells were fixed for immunofluorescence after specified intervals post-IR (0, 1, 5, 10, 20, 40, 80 min). Doses used were: 0.05, 0.1, 0.4, 1 and 2 Gy and dose rate was adjusted so that exposure times were less than 1 min for any doses. We typically refer to 'low dose' as doses below or equal to 0.1 Gy. Similarly, doses larger or equal to 1 Gy would be referred as 'high dose'. For high linear energy transfer (LET) ionizing radiation, cells were irradiated at the accelerator beam line of the NASA Space Research Lab at Brookhaven National Laboratory, with either 1 GeV/amu Fe ions or 1 GeV/amu O ions (LET = 150 kev/μm and 14 keV/μm respectively). A dose of 1 Gy was delivered at a dose rate of 1 Gy/min. ATM activity was inhibited by incubating cells with 10 μM of *ATM specific inhibitor* KU55933 (Calbiochem) from 1 hour pre-IR until cells were fixed, as previously described (12). See SI Materials and Methods for full details.

Immunostaining and Imaging

We are only briefly describing these procedures. For complete information, see supplemental information. Immunostaining using anti-53BP1 (rabbit polyclonal, Bethyl Lab. A300-272A, CA) was performed according to previous staining protocol (1). For image acquisition, both live and fixed MCF10A were imaged using a Zeiss plan-apochromat 40X dry objective (NA of 0.95) at a fixed exposure time. Non-deconvolved 3D stacks were acquired and used for image analysis (10 slices of 0.5 μm steps for fixed cells and 3 slices of 1 μm step for live cells). All image manipulations, foci analysis and statistics were done with Matlab (MathWorks, Inc., Natick, MA) and DIPimage (image processing toolbox for Matlab, Delft University of Technology, The Netherlands). In contrast to previous intensity-based methods for RIF identification (13), we used a pattern recognition approach to detect RIF by applying a wavelet morphological filter to enhance RIF peaks in the image while reducing noise from non specific signals (14). Nuclear space occupied by RIF was identified by applying a constant threshold on the wavelet filtered image and watershed algorithm was used to separate touching RIF. To test if focus size could affect the accuracy of automatic RIF detection, we applied the software on simulated data where foci sizes and densities had different values (i.e. 1 to 40 foci/nuc were simulated with four distinct sizes: 0.1, 0.4, 1.3 and 2.4 μm^3, Fig. S8). We concluded that foci overlap at the highest foci density (40 foci/nuc) will be negligible in real data and therefore will not impact RIF counts. Finally, in order to extract the number of "real" RIF from the number of background foci in each scored nucleus, we introduced a novel background subtraction method that assumes the measured RIF distribution is the result of a convolution between the "real" RIF distribution and the background foci distribution (Fig. S9). For quantification of RIF in live cells, we counted both the cumulative and instantaneous number of RIF manually in 3D time lapse images. Time interval varied between experiments and was generally set to 10 min interval for the first hour, followed by 30 min interval afterwards. This setting was optimum to minimize phototoxicity and specimen bleaching. Because of the difficulty of software to track individual foci in successive time lapse, analysis had to be done manually in a blind manner on processed images.

Mathematical Model of DSB detection and RIF formation

In order to interpret RIF kinetics in an unbiased manner, we introduce a simple mathematical model describing RIF formation where one DSB is detected at a rate k_1 leading to one RIF and one RIF is resolved after repair at a rate k_2, assuming both processes are irreversible. This model can be noted as followed: $DSB \xrightarrow{k_1} RIF \xrightarrow{k_2} RIF_{resolved}$. Let C_0 and C_1 be the average number of DSB and RIF per nucleus at time t, respectively. This kinetic model translates then into the following set of differential equations:

$$\begin{cases} \dfrac{dC_0}{dt} = -k_1 C_0 \\ \dfrac{dC_1}{dt} = k_1 C_0 - k_2 C_1 \end{cases} \Rightarrow \begin{cases} C_0(t) = C_0(0).e^{-k_1 t} \\ \dfrac{dC_1}{dt} = k_1 C_0(0).e^{-k_1 t} - k_2 C_1 \end{cases} \overset{C_1(0)=0}{\Rightarrow} \begin{cases} C_0(t) = \alpha D.e^{-k_1 t} \\ C_1(t) = \dfrac{\alpha D k_1}{k_2 - k_1}\left(e^{-k_1 t} - e^{-k_2 t}\right) \end{cases} \quad [1]$$

Where α is the number of naked DSB/Gy before formation of RIF and D is the dose delivered to the cell. α should be constant for all doses. Further details are provided in supplemental material regarding the way equation 1 is fitted. Note that one could modify the kinetic model presented here to separate rapid repair of simple lesions and slow repair of complex lesions as it has been previously suggested from PFGE DSB kinetics (15, 16). This would however lead to an additional kinetic constants, which would result in multiple solutions for the same fit. We therefore opted for a mathematical model that can be resolved with less ambiguity, using only one rate for induction and one rate for resolution.

$C_1(t)$ in equation 1 can be used to fit the number of RIF at a given time (static measure). However, one can also measure using time lapse imaging the total number of RIF that have been produced since t=0 (cumulated measure). This can be described mathematically as: $C_c(t) = \alpha D\left(1 - e^{-k_1 t}\right)$ [2]. Equation 2 is derived simply by setting k_2=0 and using the same formalism as in equation 1.

Note that the corresponding half-life for k_1 and k_2 (i.e. $t_{1/2_k}$=ln(2)/k) are reported in the text. $t_{1/2_k1}$ represents the time it takes for half of all DSB to be detected as RIF. $t_{1/2_k2}$ represents the time it takes for half of the total number of RIF to be resolved.

Acknowledgements

SVC is supported by NASA Specialized Center for Research in Radiation Health Effects [NNJ09HC64I] and the Low Dose Scientific Focus Area, United States Department of Energy [DE-AC02-05CH11231]; MB is supported by the USDOE, DOD and the NIH. TN and ST were supported by the Excellence Cluster “Nanosystems Initiative Munich". AA and DJC were supported by NASA (NNZ07AU42G).

SVC designed, supervised and partly conducted most of the experiments. Manuscript was written by SVC and MB. MB provided intellectual guidelines for designing ATM work on MCF10A. ST and TN provided support for the usage of microwell technology. Image analysis software was developed by SVC with validation and conceptual support from JS. JS and JD worked on confirming ATM inhibition was complete. TN, CP, AP, PBY participated in many of the repeats done either in the US or Germany. MB and AL provided labeled MCF10A-53BP1GFP cells for radiation experiments. AA and DJC provided movies of HT1080 used in supplemental figure.

We thank M.H. Barcellos-Hoff from NYU School of Medicine for providing earlier leadership and support and R. Sachs from UC Berkeley Math Department, J. Pluth, I. Chiolo, J. Mott, D. Ciobanu and G. Karpen from LBNL for their constructive comments on the manuscript.

References

1. Costes SV*, et al.* (2006) Imaging features that discriminate between foci induced by high- and low-LET radiation in human fibroblasts. *Radiat Res* 165(5):505-515.
2. Costes SV*, et al.* (2007) Image-based modeling reveals dynamic redistribution of DNA damage into nuclear sub-domains. *PLoS Comput Biol* 3(8):e155.
3. Rogakou EP, Pilch DR, Orr AH, Ivanova VS, & Bonner WM (1998) DNA double-stranded breaks induce histone H2AX phosphorylation on serine 139. *J Biol Chem* 273(10):5858-5868.
4. Costes SV, Chiolo I, Pluth JM, Barcellos-Hoff MH, & Jakob B (2010) Spatiotemporal characterization of ionizing radiation induced DNA damage foci and their relation to chromatin organization. *Mutat Res* 704(1-3):78-87.
5. Stenerlow B, Karlsson KH, Cooper B, & Rydberg B (2003) Measurement of prompt DNA double-strand breaks in mammalian cells without including heat-labile sites: results for cells deficient in nonhomologous end joining. *Radiat Res* 159(4):502-510.
6. Goodhead DT & Nikjoo H (1989) Track structure analysis of ultrasoft X-rays compared to high- and low-LET radiations. *Int J Radiat Biol* 55(4):513-529.
7. Erixon K & Cedervall B (1995) Linear induction of DNA double-strand breakage with X-ray dose, as determined from DNA fragment size distribution. *Radiat Res* 142(2):153-162.
8. Rothkamm K & Lobrich M (2003) Evidence for a lack of DNA double-strand break repair in human cells exposed to very low x-ray doses. *Proc Natl Acad Sci U S A* 100(9):5057-5062.
9. Asaithamby A & Chen DJ (2009) Cellular responses to DNA double-strand breaks after low-dose gamma-irradiation. *Nucleic Acids Res* 37(12):3912-3923.
10. MacPhail SH*, et al.* (2003) Expression of phosphorylated histone H2AX in cultured cell lines following exposure to X-rays. *Int J Radiat Biol* 79(5):351-358.
11. Wilson PF*, et al.* (2010) Inter-individual variation in DNA double-strand break repair in human fibroblasts before and after exposure to low doses of ionizing radiation. *Mutat Res* 683(1-2):91-97.
12. Hickson I*, et al.* (2004) Identification and characterization of a novel and specific inhibitor of the ataxia-telangiectasia mutated kinase ATM. *Cancer Res* 64(24):9152-9159.
13. Bocker W & Iliakis G (2006) Computational Methods for analysis of foci: validation for radiation-induced gamma-H2AX foci in human cells. *Radiat Res* 165(1):113-124.
14. Olivo-Marin JC (2002) Extraction of spots in biological images using multiscale products. *Pattern Recognition* 35(9):1989-1996.
15. Wang H*, et al.* (2001) Efficient rejoining of radiation-induced DNA double-strand breaks in vertebrate cells deficient in genes of the RAD52 epistasis group. *Oncogene* 20(18):2212-2224.
16. Karlsson KH, Radulescu I, Rydberg B, & Stenerlow B (2008) Repair of radiation-induced heat-labile sites is independent of DNA-PKcs, XRCC1 and PARP. *Radiat Res* 169(5):506-512.
17. Costes S, Streuli CH, & Barcellos-Hoff MH (2000) Quantitative image analysis of laminin immunoreactivity in skin basement membrane irradiated with 1 GeV/nucleon iron particles. *Radiat Res* 154(4):389-397.
18. Magee JL & Chatterjee A (1980) Radiation chemistry of heavy-particle tracks. 1. General considerations. *J. Phys. Chem.* 84:3529-3536.
19. Chatterjee A, Maccabee HD, & Tobias CA (1973) Radial cutoff LET and radial cutoff dose calculations for heavy charged particles in water. *Radiat Res* 54(3):479-494.

20. Tobias CA*, et al.* (1971) Radiological physics characteristics of the extracted heavy ion beams of the bevatron. *Science* 174(14):1131-1134.
21. Jakob B, Splinter J, & Taucher-Scholz G (2009) Positional stability of damaged chromatin domains along radiation tracks in mammalian cells. *Radiat Res* 171(4):405-418.
22. Sachs RK, Chen AM, & Brenner DJ (1997) Review: proximity effects in the production of chromosome aberrations by ionizing radiation. *Int J Radiat Biol* 71(1):1-19.
23. Sachs RK, Ponomarev AL, Hahnfeldt P, & Hlatky LR (1999) Locations of radiation-produced DNA double strand breaks along chromosomes: a stochastic cluster process formalism. *Math Biosci* 159(2):165-187.
24. Aten JA*, et al.* (2004) Dynamics of DNA double-strand breaks revealed by clustering of damaged chromosome domains. *Science* 303(5654):92-95.
25. Jakob B, Splinter J, Durante M, & Taucher-Scholz G (2009) Live cell microscopy analysis of radiation-induced DNA double-strand break motion. *Proc Natl Acad Sci U S A* 106(9):3172-3177.
26. Lisby M, Mortensen UH, & Rothstein R (2003) Colocalization of multiple DNA double-strand breaks at a single Rad52 repair centre. *Nat Cell Biol* 5(6):572-577.
27. Savage JR (1996) Insight into sites. *Mutat Res* 366(2):81-95.
28. Savage JR (2002) Reflections and meditations upon complex chromosomal exchanges. *Mutat Res* 512(2-3):93-109.
29. Anderson RM, Stevens DL, & Goodhead DT (2002) M-FISH analysis shows that complex chromosome aberrations induced by alpha -particle tracks are cumulative products of localized rearrangements. *Proc Natl Acad Sci U S A* 99(19):12167-12172.
30. Anderson RM*, et al.* (2007) Effect of linear energy transfer (LET) on the complexity of alpha-particle-induced chromosome aberrations in human CD34+ cells. *Radiat Res* 167(5):541-550.
31. Du G*, et al.* (2011) Spatial Dynamics of DNA Damage Response Protein Foci along the Ion Trajectory of High-LET Particles. *Radiat Res*.
32. Ponomarev AL, Costes SV, & Cucinotta FA (2008) Stochastic properties of radiation-induced DSB: DSB distributions in large scale chromatin loops, the HPRT gene and within the visible volumes of DNA repair foci. *International Journal of Radiation Biology* 84(11):916-929.
33. Hauptner A*, et al.* (2006) DNA-repair protein distribution along the tracks of energetic ions. *Radiat Prot Dosimetry* 122(1-4):147-149.
34. Nikjoo H, O'Neill P, Goodhead DT, & Terrissol M (1997) Computational modelling of low-energy electron-induced DNA damage by early physical and chemical events. *Int J Radiat Biol* 71(5):467-483.
35. Nikjoo H, O'Neill P, Wilson WE, & Goodhead DT (2001) Computational approach for determining the spectrum of DNA damage induced by ionizing radiation. *Radiat Res* 156(5 Pt 2):577-583.
36. Kato TA, Okayasu R, & Bedford JS (2008) Comparison of the induction and disappearance of DNA double strand breaks and gamma-H2AX foci after irradiation of chromosomes in G1-phase or in condensed metaphase cells. *Mutat Res* 639(1-2):108-112.
37. Leatherbarrow EL, Harper JV, Cucinotta FA, & O'Neill P (2006) Induction and quantification of gamma-H2AX foci following low and high LET-irradiation. *Int J Radiat Biol* 82(2):111-118.
38. Bakkenist CJ & Kastan MB (2003) DNA damage activates ATM through intermolecular autophosphorylation and dimer dissociation. *Nature* 421(6922):499-506.
39. Baure J*, et al.* (2009) Histone H2AX phosphorylation in response to changes in chromatin structure induced by altered osmolarity. *Mutagenesis* 24(2):161-167.
40. Chiolo I*, et al.* (2011) Double-strand breaks in heterochromatin move outside of a dynamic HP1a domain to complete recombinational repair. *Cell* 144(5):732-744.

41. Jakob B*, et al.* (2011) DNA double-strand breaks in heterochromatin elicit fast repair protein recruitment, histone H2AX phosphorylation and relocation to euchromatin. *Nucleic Acids Res* 39(15):6489-6499.
42. Costes S*, et al.* (2001) Large-mutation spectra induced at hemizygous loci by low-LET radiation: evidence for intrachromosomal proximity effects. *Radiat Res* 156(5 Pt 1):545-557.
43. Brenner DJ & Sachs RK (2006) Estimating radiation-induced cancer risks at very low doses: rationale for using a linear no-threshold approach. *Radiat Environ Biophys* 44(4):253-256.

Table I. Fitted parameters for various doses of X-rays, and for Delta-rays and track core time response to 1 Gy of 1 GeV/amu Fe

Dose (Gy)	AVERAGE			STANDARD ERROR		
	α (RIF/Gy)	T1/2_1 (MIN)	T1/2_2 (HR)	α (RIF/Gy)	T1/2_1 (MIN)	T1/2_2 (HR)
CONTROLS MCF10A (N=7)						
0.1	64	5.6	1.4	6	1.3	0.5
0.4	38	3.4	2.0	2	0.4	0.6
1	23	2.8	3.8	3	0.5	0.6
2	15	2.4	5.7	2	0.1	1.6
ATM INHIBITION MCF10A (ONE EXPERIMENT)						
0.1	25	8.3	0.7	17	5.8	0.5
0.4	25	5.9	3.5	4	1.1	0.6
1	19	4.2	8.7	2	0.5	1.1
2	12	2.6	15.4	2	0.3	1.9
LIVE 53BP1-GFP IN MCF10A (N=3, 5 to 10 cells per experiment)						
0.1	73	15.4	1.4	5	1.6	0.2
1	28	6.5	2.1	3	2.1	0.1
1 GeV/amu Fe in MCF10A (N=5)						
0.17 (Delta-rays)*	43	2.8	3.3	9	0.2	0.8
27 (core)*	--	0.1	9.6	--	0.01	1.6

*Dose estimation, based on microdosimetry computations of 1GeV/amu Fe exposure (Fig. S4)

Figures

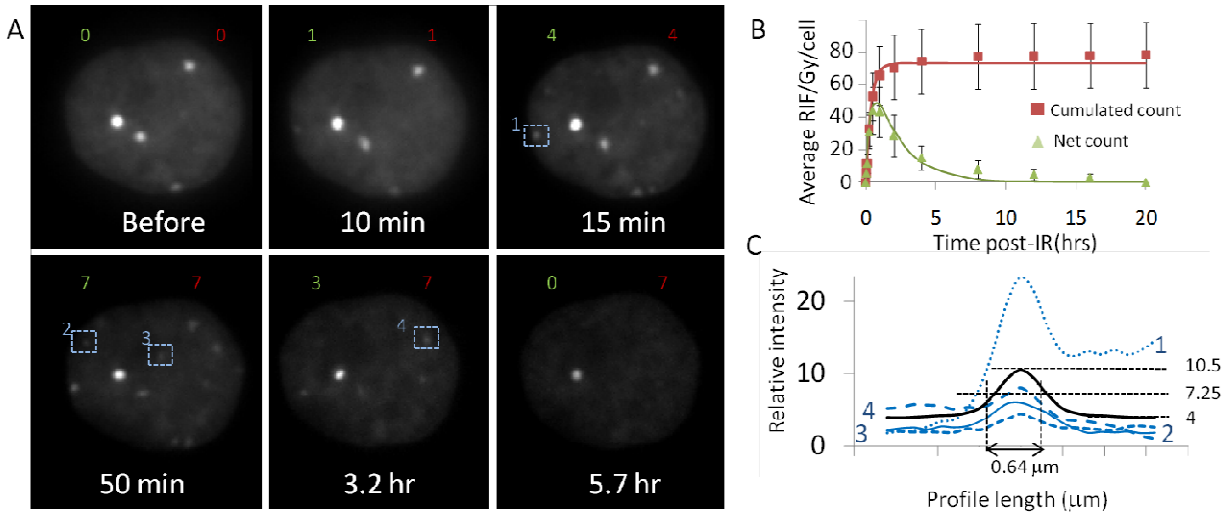

Fig. 1: Time lapse imaging of MCF10A transiently transfected with 53BP1-GFP after exposure to 0.1 Gy of X-rays. **(A)** representative snapshots of best focal plane for a 3D time lapse. Counting was done manually in two different ways: 1. static measurement, indicating the number of RIF/cell at the time it is measured (green numbers and graphs). 2. cumulated measurement, indicating at any time the overall number of different RIF that have appeared since time 0 (red numbers and graphs). 53BP1 nuclear bodies visible before IR were not included in RIF counts. **(B)** RIF counts from 40 different time lapses (3 independent experiments) leads to an average for $T_{1/2_induction}$= 15 min, $T_{1/2_resolution}$= 1.4 hr, α=73 RIF/Gy. Fits are shown as solid lines and experimental points as red square for cumulated counts and green triangles for net counts (R^2 =0.98 and t-test P-value=0.005 for the fit). **(C)** 1D intensity profiles of 4 different regions of interest indicated by blue dash box in panel (A). The average profile is indicated by solid curve and used to evaluate the average size of a focus (defined as the full-width-half-max of the peak).

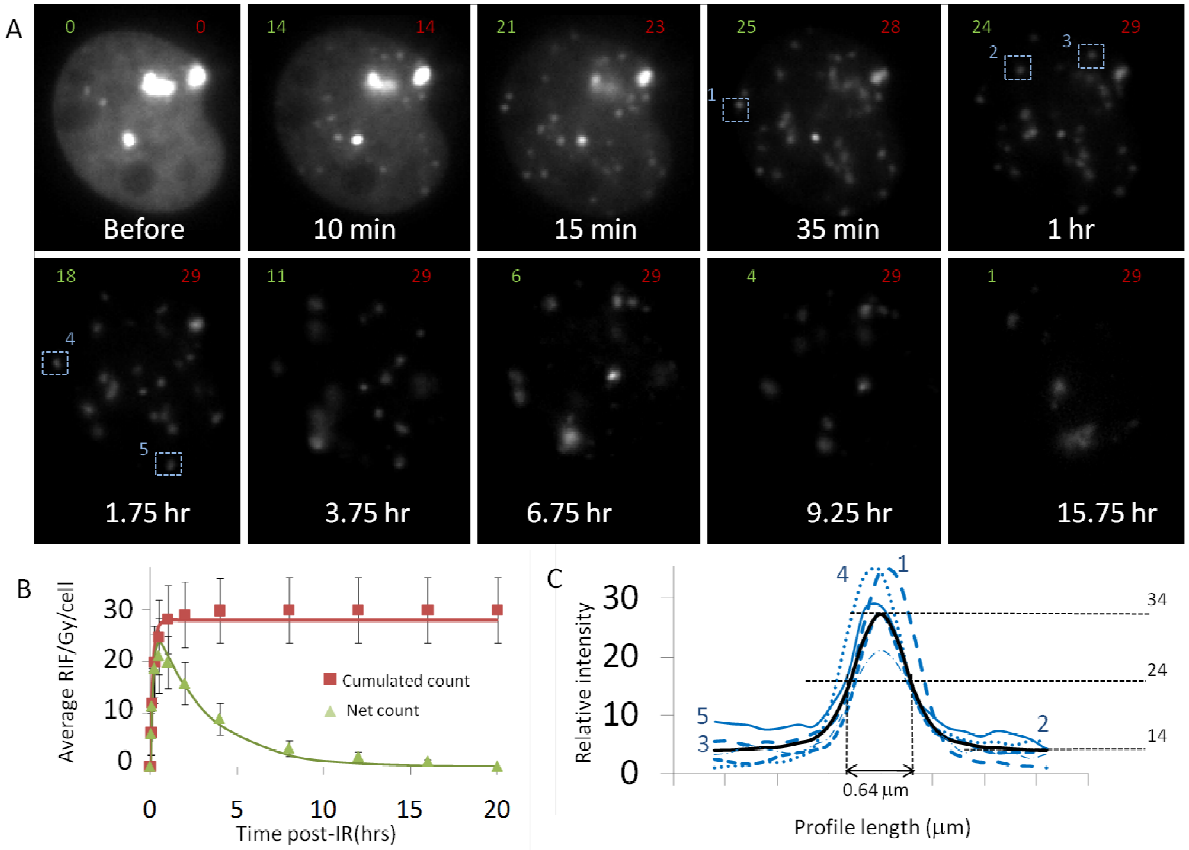

Fig. 2: Time lapse imaging of MCF10A transiently transfected with 53BP1-GFP after exposure to 1 Gy of X-rays. **(A)** representative snapshots of best focal plane for a 3D time lapse. **(B)** RIF counts from 21 different time lapses (3 independent experiments) leads to an average for $T_{1/2_induction}$= 6.5 min, $T_{1/2_resolution}$= 2.1 hr, α=28 RIF/Gy. R^2 =0.99 and t-test P-value=0.003 for the fit. **(C)** 1D intensity profiles of 4 different regions of interest indicated by blue dash box in panel (A).

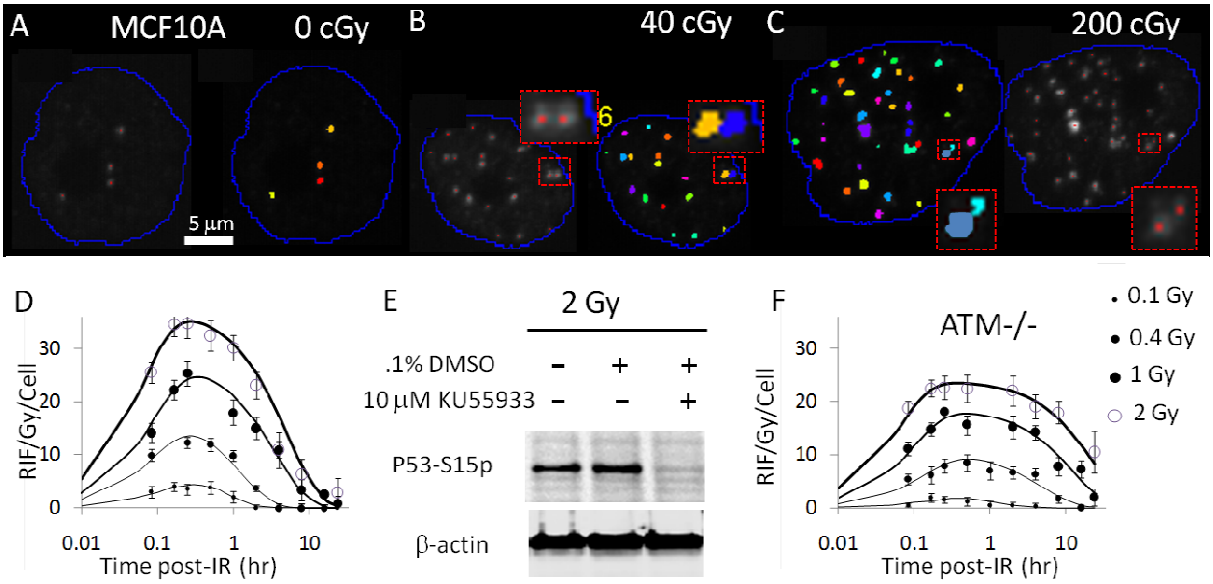

Fig. 3: Representative time response of background corrected RIF per nucleus in MCF10A exposed to various doses of X-rays and immunostained for 53BP1. Experimental data points (circles) get larger with dose (0.1, 0.4, 1 and 2 Gy respectively) and they correspond to averages for ~1000 nuclei per point, with their corresponding standard deviations. Solid lines are least square fits using equation 1 for each time response. **(A,B,C)** Maximum intensity projections of representative 3D stack images at various doses (red dots indicate detected 53BP1 RIF) are accompanied with the same nucleus overlaid with the full shape identification of a RIF and the ability of the algorithm to separate touching RIF even at the maximum dose (panel D - 2 Gy, see enlargement). In these images, each RIF is labeled by the algorithm with a different color to facilitate individual visualization. (D) Time response under normal media conditions for one experiment out of 7 performed (average R^2 across all doses is 0.98 and t-test P-value is less than 0.01). (E) Inhibition of ATM measured by Western Blot of P53-S15p. (D) Time response under ATM inhibition (average R^2 across all doses is 0.99 and t-test P-value is less than 0.01), based on one experiment.

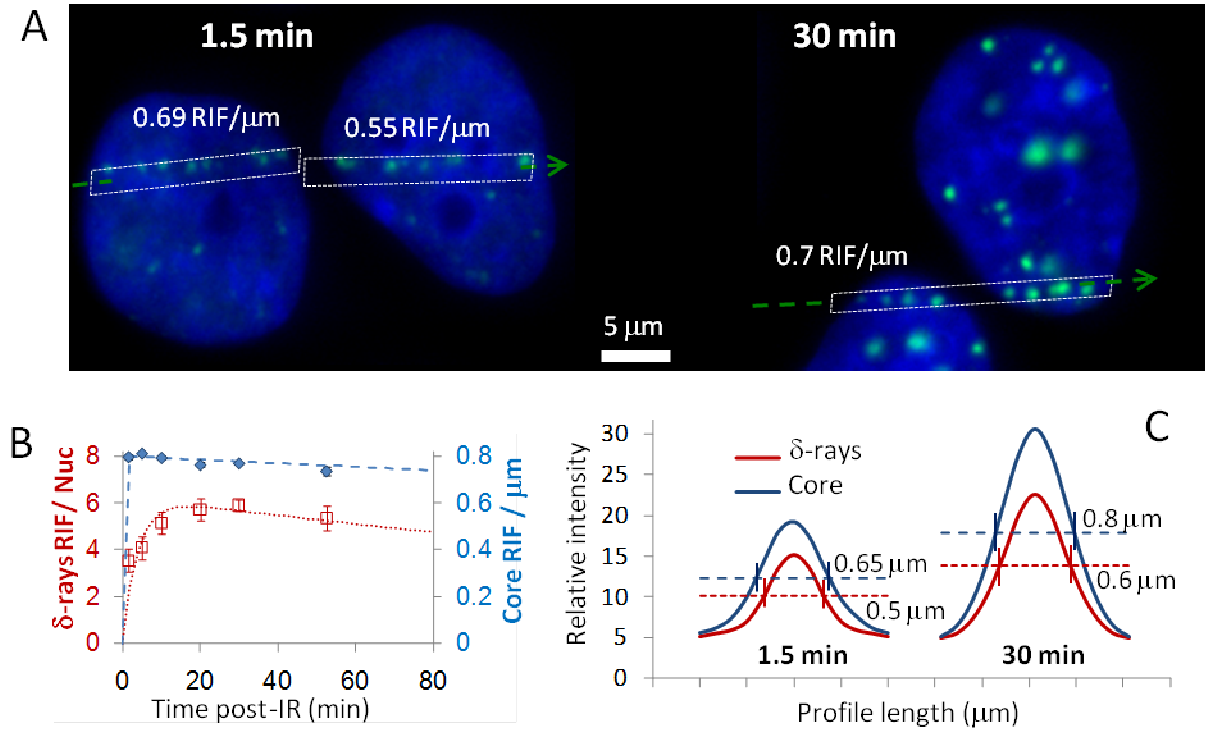

Fig. 4: Representative time response of background corrected RIF per nucleus in MCF10A exposed to 1 GeV/amu Fe ions and immunostained for 53BP1. (A) Representative images for 1.5 and 30 min post-IR, illustrating which RIF are classified "core RIF" vs "Delta-rays RIF". **(B)** Time response averaged over 5 independent experiments cumulating more than 1000 tracks per time-point and experiment. Delta-rays RIF are reported as RIF/nuc/Gy (red), where as core RIF are reported as RIF/µm (blue). **(C)** Average normalized intensity profiles at 1.5 and 30 min post-IR for core and deltay-rays RIF (N=20 for each profile - RIF diameters are shown as the full-width-half-max of the peaks).

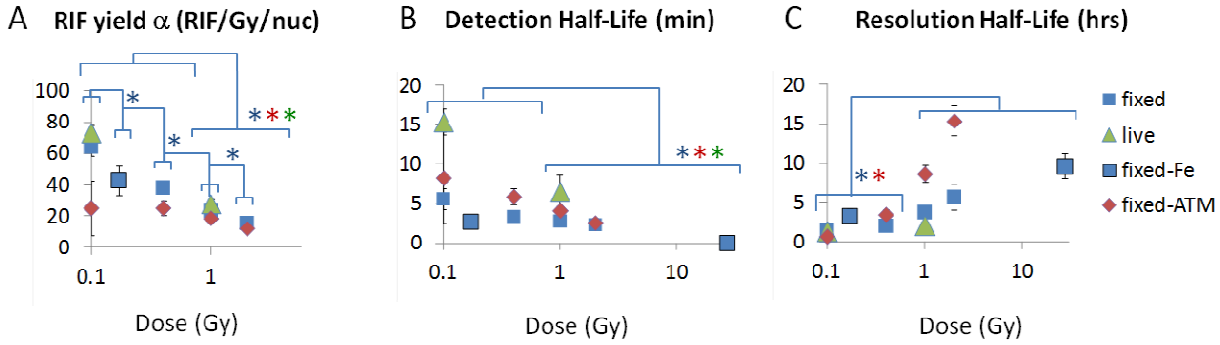

Fig. 5: Average fitted parameters for all time responses measured in human MCF10A. Four conditions are considered (**fixed**: normal condition, immunostaining of 53BP1, N=7; **fixed-ATM**: ATM inihibition and immunostaining of 53BP1, N=1; **fixed-Fe** 53BP1 immunostaining after exposure to 1 GeV/amu Fe, with estimated doses along ion tracks of 26 Gy and outsitde tracks of 0.17 Gy, N=5; **live:** time lapse imaging of MCF10A transiently transfected with 53BP1-GFP after exposure to 0.1 and 1 Gy of X-rays, N=3). All trends are statistically significant with respect to dose using one way ANOVA test ($P<0.01$ for α and $P<0.05$ for k_1 and k_2). Statistical

differences between dose points are tested with the Tukey-Kramer test and are indicated by an asterisk with the color corresponding to the group when significant. (A) Absolute RIF yield α (RIF/Gy/nucleus), showing a decrease with dose. (B) RIF induction half-life ($\ln(2)/k_1$), showing a faster induction with dose. (C) RIF disappearance-resolution half-life ($\ln(2)/k_2$) showing a slower RIF resolution with dose.

SI Text

Materials and Methods

Cell culture

Adherent growing human foreskin diploid fibroblasts, HCA2 were cultivated in minimum essential medium (MEM) alpha (Invitrogen Inc., Carlsbad, CA), supplemented with 10% fetal bovine serum. Human mammary epithelial cells, MCF10A obtained from ATCC, were grown in MEMB media supplemented with bovine pituitatry hormone (13mg/ml), hydrocortisone (0.5mg/ml), hEGF (10µg/ml), insulin (5mg/ml) and cholera toxin (100ng/ml) (Invitrogen Inc., Carlsbad, CA). Both cell lines were cultivated at 37°C, with 95% humidity and 5% CO_2. For experiments, both cell lines were seeded either in Permanox plastic 8-well Lab-Tek chamber slides (Nalge Nunc International Corp., Rochester, NY) or on 48 hydrophilic spots of functionalized glass-slides (AmpliGrid, Beckman Coulter GmbH, Krefeld, Germany). The cells were cultivated to a confluent layer prior to irradiation. HT1080 and human bronchial epithelial cells (HBEC) were grown and maintained as previously described (1). For live cell imaging, HT1080 and HBEC were stably transfected with 53BP1-GFP (1), whereas MCF10A were transiently transfected with H1.5-DsRed2 and 53BP1-GFP using lipofectamine LTX (Invitrogen). H1.5-DsRed2 for chromatin labelling that was generously given by Dr. Michael Hendzel from the University of Alberta, Canada. DNA damage labelling was done with 53BP1-GFP construct, generously given by Dr. Thanos Halazonetis from the University of Geneva, Switzerland.

Irradiation

Identical dose- and time-response experiments were conducted with cells exposed to X-rays (160kV or 320 kV) to optimize the immunostaining of radiation-induced foci. For the optimization experiments cells were irradiated with 100 cGy of X-ray and fixed after 30 min repair time to get a maximum RIF induction as previously shown (2). For the matrix experiments with different doses and time-responses, cells grown on one functionalized glass slide were irradiated with two doses. Therefore, one part of the modified glass slide was shielded with lead. Furthermore, the sample was placed on top of lead to minimise backscattering. Cells in each well were fixed at different time and dose points (0, 1, 5, 10, 20, 40, 80 min post-IR/0, 5,10, 15, 40, 50, 100, 200 and 400 cGy) on a warm block and returned to the 37°C incubator. Dose rates were

modified as little as possible for each dose as long as the exposure time was less than one minute to get accurate early time-points, and was more than 10 sec for accurate determination of the dose. This led to three different dose rates: 450 cGy/min for 200 and 400 cGy; 150 cGy/min for 100, 50 and 40; 30 cGy/min for 5, 10 and 15 cGy. For high-LET radiation, cells were irradiated at the accelerator beam line of the NASA Space Research Lab at Brookhaven National Laboratory, with either 1 GeV/amu Fe ions or 1 GeV/amu O ions (LET = 150 kev/µm and 14 keV/µm respectively). A dose of 1 Gy was delivered at a dose rate of 100 cGy/min.

Immunostaining

Two different culture platforms were evaluated (i.e. 48 microwell ampligrid vs. 8 well chamber slides). Immunostaining was optimized using cells exposed to 100 cGy of X-rays and fixed 30 min after irradiation with 2% paraformaldehyde in PBS for 15 min at room temperature followed by permeabilization with 100% ice-cold methanol for 15min at –20°C. Subsequently blocking, primary antibody incubation and secondary antibody incubation were optimised through titration experiments. The rest of the staining was performed according to the conventional staining protocol (2) but with BSA used for blocking instead of casein supernatant. When cells were grown on AmpliGrids, optimization was performed reducing the immunostaining time less than one hour. By using 5 µl of reagent for each incubation step in the microwells, we could increase antibody concentration with no significant impact on cost. Briefly, titration times for the optimization were 1, 2, 4, 8, 16, 32 or 64 min as well as additional 128 min for the primary antibody. The primary antibodies were either a rabbit polyclonal anti 53BP1 antibody (stock at 1 mg/ml, Bethyl Laboratories, San Francisco, CA) or a mouse monoclonal to phospho-histone H2AX antibody (stock at 1 mg/ml, clone JBW301; Upstate Cell Signalling Solutions Inc. Charlottesville, VA). The corresponding secondary antibodies were either FITC labelled anti-rabbit IgGs or, FITC or T-Red labelled anti-mouse IgGs (Molecular Probes Invitrogen, Carlsbad, CA). After three washing steps with PBS at room temperature, cells were either blocked with 0,1% BSA for 1h for the antibody titers or the blocking titer was performed with 0,1%, 0,2% and 1% BSA at room temperature. The samples of the blocking titer were incubated with the primary antibody for 2 h and then, after extensive washing with PBS, incubated with the secondary antibody for 1h. The other samples were either incubated with the primary antibody for 2 h and, subsequently, used for the secondary antibody titer, or the primary titer with the dilutions 1:10, 1:100, 1:200 was performed at room temperature. The primary titer samples were washed extensively with PBS after the titration and then incubated with the secondary antibody for 1 h. The secondary antibody titer samples were also washed with PBS before the secondary antibody titration was performed. Dilutions used for the secondary antibody incubation optimization were 1:10, 1:100, 1:200. After a further washing step with PBS the samples were counterstained with DAPI and then analyzed with regard to foci intensity.

By plotting the relative foci intensities against time, saturation of the relative foci intensities was observed after a short time for all concentrations and dilutions. Saturation was reached for the blocking titration between 8 – 16 min in dependence on the BSA concentration. For the primary antibody the saturation was always reached after 16 min independent from the antibody concentration. The secondary antibody plot showed more variations in the saturation time-points in dependence on the antibody concentration. Saturation was obtained after 32 min for the 1:200 antibody dilutions, after 16 min for the 1:100 dilution and after 8 min for the 1:10 dilution. Fig. S7A shows the progression of the curves for the 1:100 dilution for both antibodies and the curve for the 1% BSA solution. The curve progressions as well as the intensity of the microscopic images led to the conclusion that longer incubation does not improve the quality of the images. Indeed, longer blocking results in lower foci intensities (Fig. S7B). For both antibodies the saturation in the foci intensity can also be seen in the microscopic images (Fig. S7C and D). The saturation of the titration curves observed as well as the quality of the images led to the decision to reduce the incubation time for the three staining steps to 15 min for the three reagents and to use a 0.2% concentration of BSA and 1:100 dilutions for both antibodies in the matrix experiments. Corresponding images for these incubation times and dilution are shown in Fig. S7E, clearly showing the improvement in image quality compared to other conditions (Fig. S7B - D).

Image Acquisition

Cells were viewed and imaged using a Zeiss Axiovert 200M automated microscope with Ludl position-encoded scanning stage (Carl Zeiss, Jena, Germany). Images were acquired using a Zeiss plan-apochromat 40X dry objective (NA of 0.95) and a very sensitive scientific-grade EM-CCD camera (Hamamatsu C9100-02, 1k by 1k pixels, , 8 x 8 μm^2 pixels). The image pixel size was measured to be 0.2 μm but based on the NA of the objective, the actual resolution of the image in the FITC channel is ~ 0.5x0.488/NA = 0.26 μm. All images were captured with the same exposure time so that intensities were within the 16-bit linear range and could be compared between specimens. For 3D data set, a CSU-10 spinning disk confocal scanner was used to acquire optical slices of 0.5 μm thickness and illumination was provided by 4 solid-state lasers at 405, 491, 561, and 638 nm under AOTF control. For 2D data set, simple conventional image was taken with the same optics but without spinning disk. Finally, a multiband dichroic and single-band emission filters in a filterwheel selected the fluorescent light captured by the camera, removing any type of bleedthrough between channels. For X-ray experiments on live HT1080, time-lapse imaging was carried out as previously described (1), using an LSM 510 Meta laser

scanning confocal microscope (Carl Zeiss, Jena, Germany) with a 63X 1.4 NA Plan-Apochromat oil immersion objective.

Cell cycle considerations

We noted that MCF10A are not fully arrested at confluence and thus we corrected for high foci count from cells in G2 or S-phase as previously described (2): briefly, foci counts were scaled to represent the number of foci for the same size nucleus, using the G1 nuclear volume as the reference nuclear volume. DAPI content and EdU pulsing (Click-iT®, Invitrogen) were used to estimate proportions of cells in each phase. Note that cells in late G2 are problematic as 53BP1 signals becomes weaker with a signal fully cytoplasmic during mitosis, leading to complete loss of foci until reentry in G1. However, this effect should have very little impact on the analysis as only 5% of cells were in G2 and less than 1% in mitosis. We also measured 9% of the cells being in S-phase, which could lead to higher foci background due to stalled replication forks. However, working with 53BP1 alleviated this problem, as background issues have been reported primarily with γH2AX not 53BP1 (2).

Image Analysis of live cells

Processing of 3D time lapse was done by first applying a maximum intensity projection (MIP) on all Z stack to allow visualization of all foci within one single plane. This first step resulted in the generation of 2D time lapse which could then be realigned between time points on a per nucleus basis (translation and rotation), to help distinguishing foci movement from foci formation or resolution. Various doses of X-rays were considered (0.05, 0.1 and 1 Gy) for a kinetic covering 5 min to 20 hours post-IR, depending on the cells used. 3D time lapse were acquired and averaged over 20 and 40 cells for each dose. RIF size for live cell imaging was obtained by computing the full width half-max determined by a 1D intensity profile crossing the center of the RIF. The cross section was done manually, and the reported size only reflected the average diameter of the RIF.

Impact of foci size and foci density on foci detection

Nuclear space occupied by RIF was identified by applying a constant threshold on the wavelet filtered image and watershed algorithm was used to separate touching RIF. To test if focus size could affect the accuracy of automatic RIF detection, we applied the software on simulated data where foci sizes and densities had different values (i.e. 1 to 40 foci/nuc were simulated with four distinct sizes: 0.1, 0.4, 1.3 and 2.4 μm^3, Fig. S8). We concluded that foci overlap at the highest foci density (40 foci/nuc) will be negligible in real data and therefore will not impact RIF counts.

When foci were all as large as 1.3 or 2.4 μm^3, we started computing number of foci/nuc lower than simulated (i.e. 10 and 25% lower than expected respectively, when simulating 40 foci/nuc). It is interesting to note in that situation the algorithm reported lower sizes than simulated as well. This reflects the ability of the algorithm to separate touching foci, minimizing the impact of foci overlap. Since RIF sizes are on average much lower (i.e. 95% of RIF sizes in a real specimen exposed to 1 Gy are below 1 μm^3 - Fig. S8A), and the minimum detectable focus size is ~0.1 μm^3, simulations suggest that foci overlap at the highest foci density (40 foci/nuc) will be negligible in real data and therefore will not impact RIF counts. Finally, in order to extract the number of "real" RIF from the number of background foci in each scored nucleus, we introduced a novel background subtraction method that assumes the measured RIF distribution is the result of a convolution between the "real" RIF distribution (i.e. assumed to be Poisson) and the background foci distribution (full details on the methods are given in supplemental material and Fig. S9). For quantification of RIF in live cells, we counted both the cumulative and instantaneous number of RIF manually in 3D time lapse images. Time interval varied between experiments and was generally set to 10 min interval for the first hour, followed by 30 min interval afterwards. This setting was optimum to minimize phototoxicity and specimen bleaching. Because of the difficulty of software to track individual foci in successive time lapse, analysis was done manually in a blind manner on processed images.

Background foci correction

The human cells we used have significant amount of background foci. In this work, we introduced a method to correct for their presence in irradiated specimen. Briefly, we know that DNA damages are random events taking place in a specified unit of space (the nucleus) with an average frequency Φ (RIF/nuc). Therefore, the probability of having N hits in a given cell is defined by the Poisson distribution $Pois(N,\Phi)$. If we were to measure the number of cells with N RIF after exposure of a dose D, this would lead to the distribution $H(N,D) = H(N,0) \otimes Pois(N,\Phi)$, where $H(N,0)$ is the distribution of background foci without radiation. In other words, the measured distribution of RIF/nucleus in a specimen should be a Poisson distribution whose means is the average number of RIF/nucleus convolved with the distribution of background foci present before exposure to ionizing radiation. For each measured distribution $H(N,D)$, we searched the value of Φ that yielded the best fit by incremental changes on Φ.

If the Poisson assumption is right, such method should lead to more accurate values for RIF estimation (i.e. fitting with a mathematical function is less sensitive to noise than computing the average). High R squared values between the fits and the measured distributions were indeed observed (average R^2~0.92, Fig. S9), validating the assumption that "real" RIF are distributed randomly among nuclei, much like DSB. This background correction worked well down to 0.15

Gy (average R^2~0.93). However, 0.05 Gy exposures led to distributions that could not be fitted with high statistical significance, a problem that might be overcome with much larger sample sizes. We are therefore only reporting RIF frequencies for doses ≥ 0.15 Gy. One should also note that correcting the measured number of RIF by only subtracting the mean number of background foci could not have been fitted well by a Poisson distribution due to the non-Poisson contribution of background foci (green curve, Fig. S8, upper panel). It is known that background foci changes with each cell cycle and the non normal distribution probably reflects the various cycle distribution. Therefore, such traditional method would not have permitted us to conclude on the random distribution of RIF.

References

1. Asaithamby, A. and Chen, D.J. (2009) Cellular responses to DNA double-strand breaks after low-dose gamma-irradiation. *Nucleic Acids Res*, **37**, 3912-3923.

2. Costes, S.V., Boissiere, A., Ravani, S., Romano, R., Parvin, B. and Barcellos-Hoff, M.H. (2006) Imaging features that discriminate between foci induced by high- and low-LET radiation in human fibroblasts. *Radiat Res*, **165**, 505-515.

\ SUPPLEMENTAL FIGURES LEGENDS

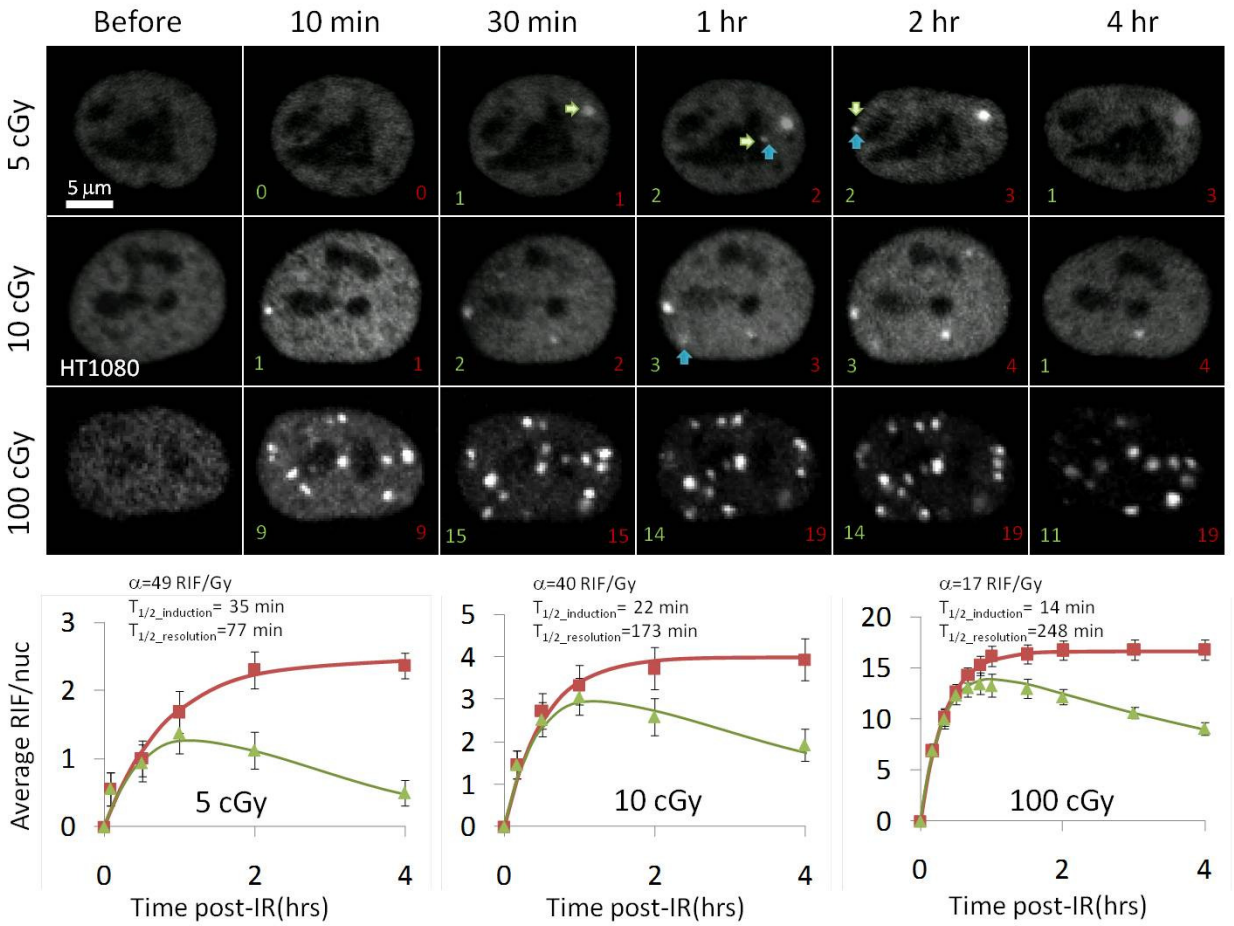

Fig. S1: Time lapse imaging of human fibrosarcoma HT1080 stably transfected with 53BP1-GFP. Upper panels show representative snapshots of movies for three different doses (5, 10 and 100 cGy). Counting was done manually and done in two different ways: 1. static measurement, indicating the number of RIF/cell at the time it is measured (green numbers and graphs). 2. cumulated measurement, indicating at any time the overall number of different RIF that have appeared since time 0 (red numbers and graphs). The lower panel shows the average of these counts from 20-40 nuclei per dose (red square for cumulated averages and green triangles for static averages). Static and cumulated averages could be fitted simultaneously with the same parameters using equation 1 and 2 respectively.

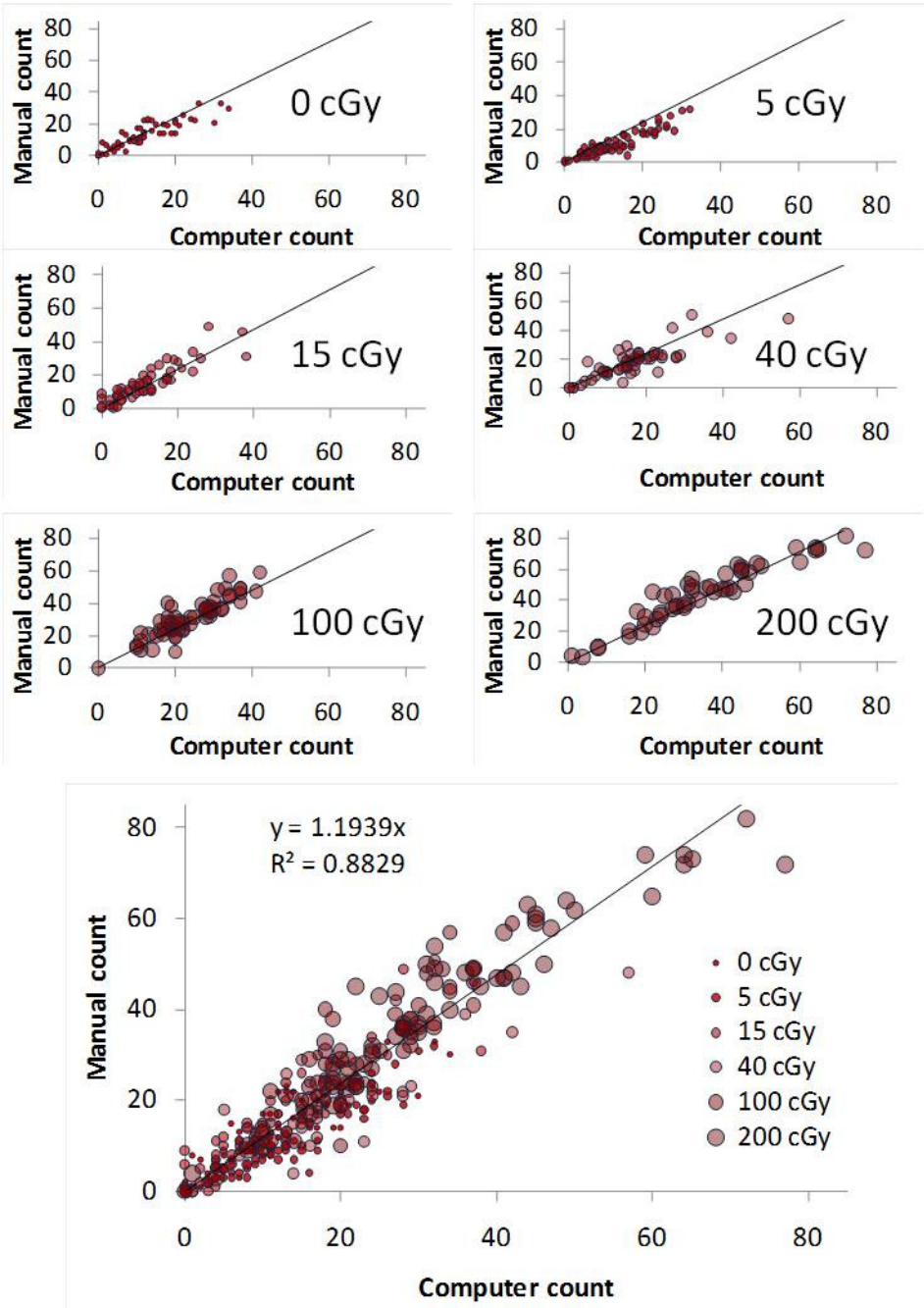

Fig. S2: Human validation of spot detection algorithm. Human mammary epithelial cells (MCF10A) were exposed to various doses of X-rays, immunostained for 53BP1 and RIF were counted manually or by algorithm from 3D stacks. Graph plotting RIF counts scored by computer algorithm against RIF counts scored blindly by human eye for various doses show good agreement. A total of 350 nuclei were scored here and each nuclear count is represented as a circle, with circles of larger sizes for larger doses. Linear regression led to an overall $R^2 = 0.88$ and P-value for t-test less than 0.05 (lower graph), indicating good agreement between manual and automatic counts.

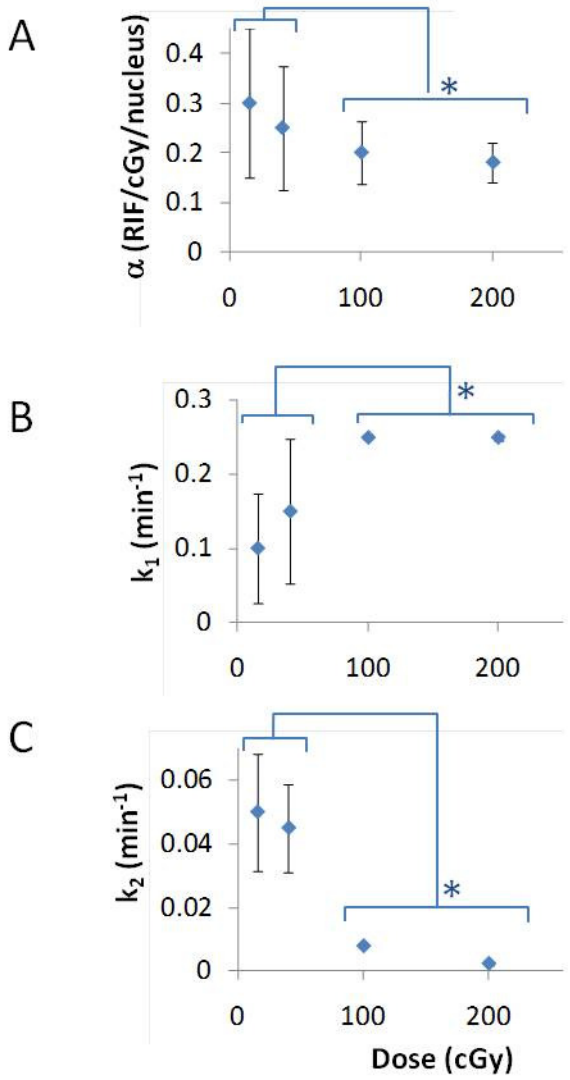

Fig. S3: RIF dose-kinetic fits from single experiment performed on normal human skin diploid fibroblasts in G1 (HCA2) imaged by 3D microscopy and stained for 53BP1. (A) Absolute RIF yield α (RIF/Gy/nucleus), showing a decrease with dose. (B) RIF induction kinetics constants (k_1), showing a faster induction with dose. (C) RIF disappearance-resolution kinetics constants (k_2) showing a slower RIF resolution with dose. Note that since only one experiment was performed here, error bars represent standard deviations from measurements made over 3000 nuclei per dose point. Trend significance using t-test between [0.1,0.4] Gy group and high dose group and using duplicate well as separate measurements ($P<0.05$) are shown by asterix.

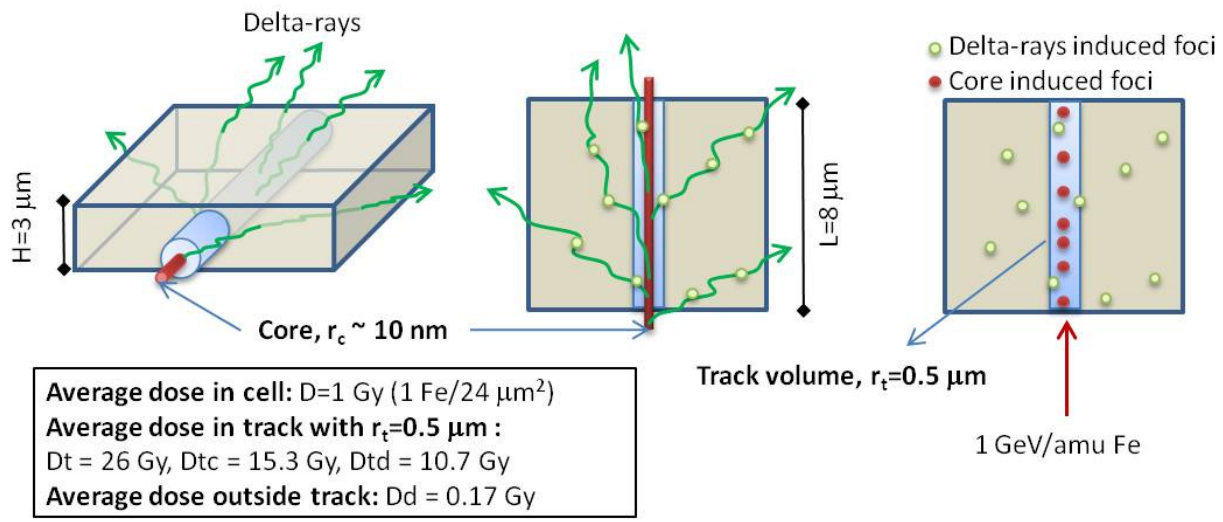

Fig. S4: Illustration of energy deposition from HZE particle 1 GeV/amu Fe ion in a theoretical rectangular cell. A small red cylinder crossing the cell in the middle along its length indicates the core of the HZE. Delta-rays generated in the core via Coulomb interactions are depicted as green arrows.

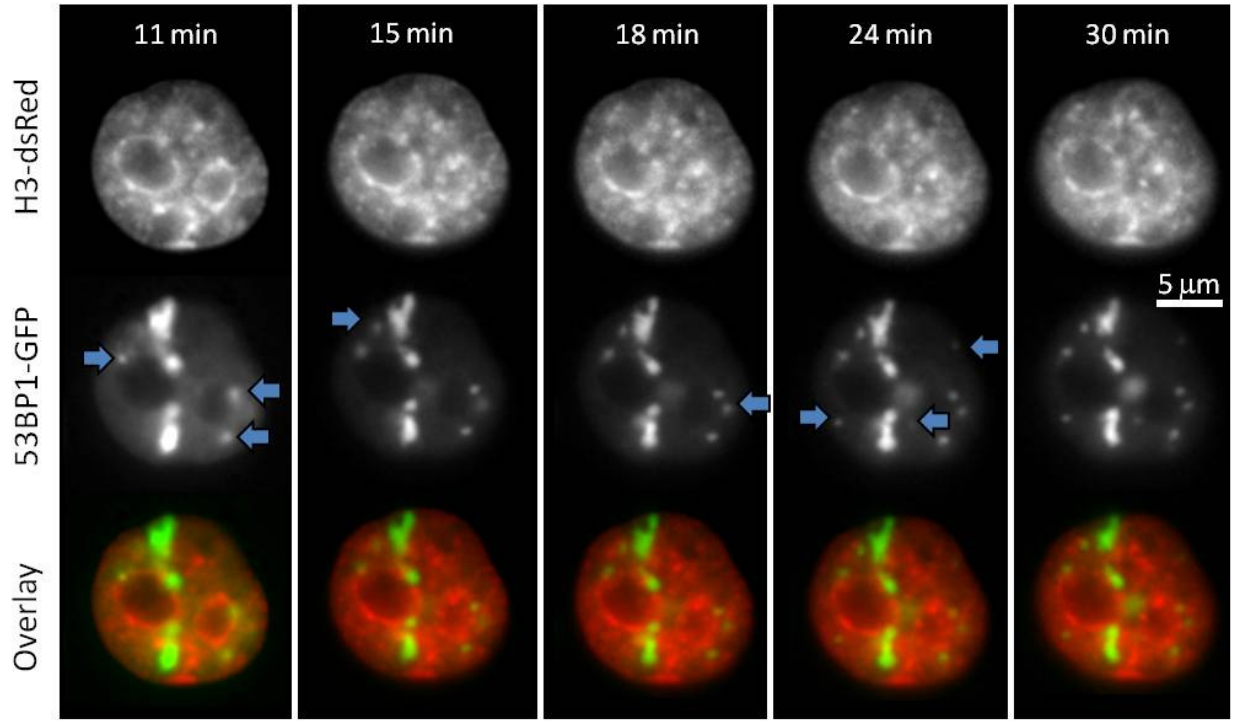

Fig. S5: Time lapse imaging of MCF10A exposed to 1 track of 1 GeV/amu Fe ion (~0.24 Gy, LET~148 keV/µm). Cells are transiently transfected with 53BP1-GFP RIF and H3-dsRed. Time lapse confirms delayed kinetics for the apparition of low-LET RIF (appearing delta-rays RIF are indicated by blue arrows in each time frame). Track RIF frequency here is ~0.65 RIF/µm across

the time-points 11 to 30 min post-IR, whereas low-LET RIF frequencies reach a maximum between 24 and 30 min post-IR.

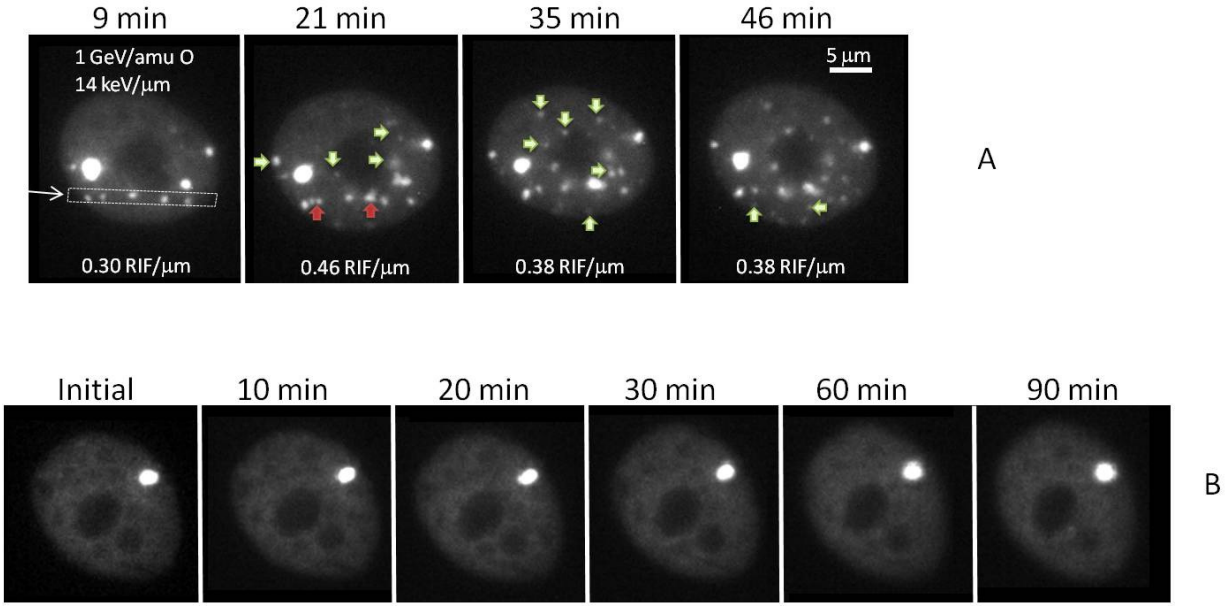

Fig. S6: (A) Stably transfected human bronchial epithelial cells (HBEC) exposed to 1 track of 1 GeV/amu O ions (~0.022 Gy, LET~14 keV/μm). (B) Control HBEC which did not get irradiated show no induction of foci for similar time lapse acquisition frequency. This confirms that delayed foci appearing in panel A are not the result of photodamage from imaging.

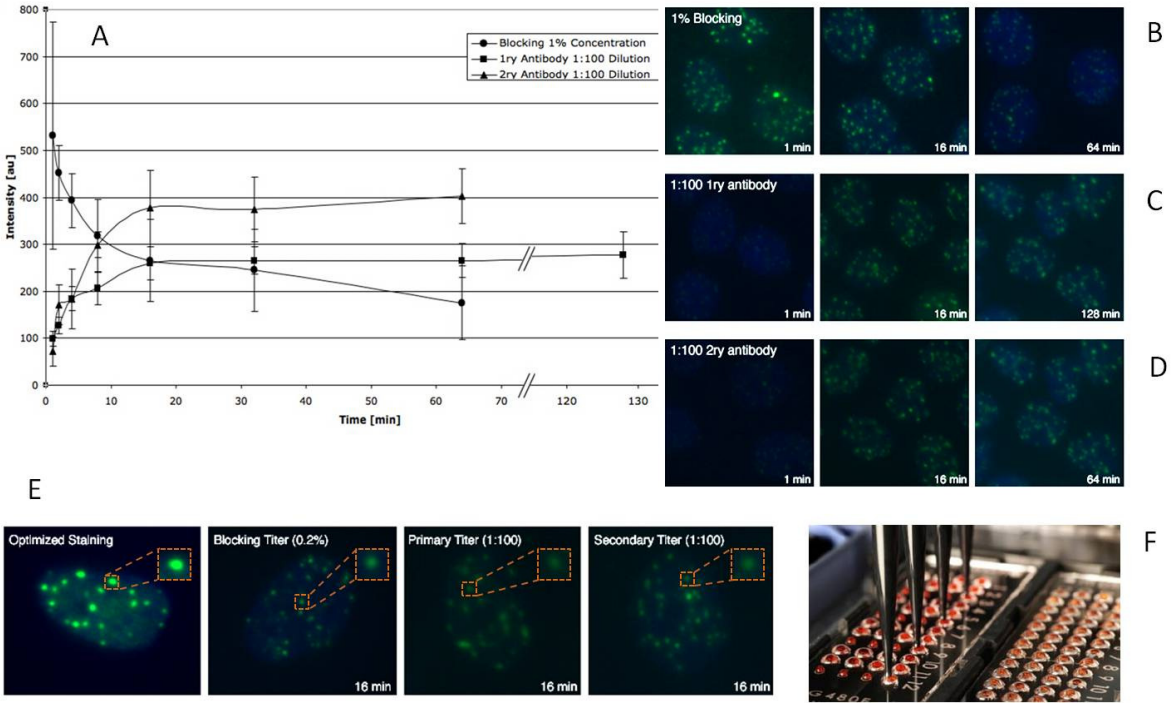

Fig. S7: Immunofluorescence (IF) staining optimization. Optimization of 53BP1 staining was performed for the concentrations and incubation times of 3 parameters: i) the blocking agent (BSA), ii) the primary antibody (1° Ab) and iii) the secondary antibody (2° Ab). The un-optimized staining protocol was blocking with 0.1% BSA (1Hr), incubation with 1° Ab (1:200, 1Hr) and 2° Ab (1:200, 2Hr). (A) IF intensities of 53BP1 staining for various incubation times of the 1° and 2° Ab (using optimized Ab concentrations). The relative foci intensities saturate for all conditions after about 16 min. This indicates short incubation times (~15-20 min), with higher concentrations of Ab (1:100) is enough for optimum results. This conclusion is supported by visual analysis of the microscopic images, as is the effect of combining each optimized parameter, which appears additive (B-E) . Panel (F) shows one ampligrid.

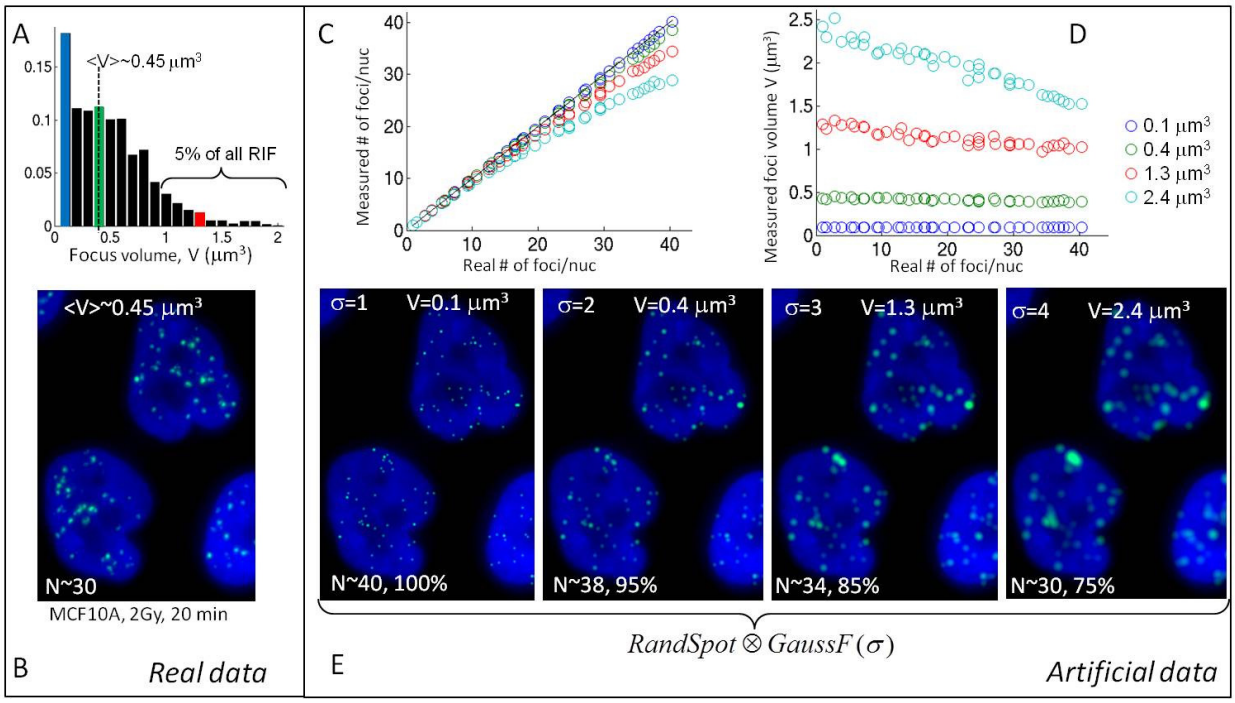

Fig. S8 : Impact of foci sizes on detection. (A) Distribution of 53BP1 RIF volumes after 2 Gy of X-rays in MCF10A. (B) Representative maximum intensity projection (MIP) is shown below the graph. The average focus volume for this time point is 0.45 μm^3. The distribution indicates that 95% of RIF have volumes lower than 1 μm^3. (C-E) Using the same set of nuclei, random spots were generated in the 3D volumes defined by each nucleus from an average of 1 to 40 foci/nucleus. The same spots were expanded using a Gaussian filter with various sigma values (σ = 1, 2, 3, 4) leading to various foci volumes (0.1, 0.4, 1.3 and 2.4 μm^3, respectively). The position of each of this foci volumes are depicted with the same color on the distribution graph in (A - except 2.4 μm^3 which is off the chart). (C) shows that for 1.3 and 2.4 μm^3 foci, detection is statistically lower than reality when the average number of foci/nucleus is greater than 30 and 20 respectively. (D) shows the reported foci volume as a function of the number of foci/nucleus for different simulated foci volumes. One can note that the algorithm can maintain accurate count by reducing the reported volume of the foci. (E) shows MIP of the corresponding images for these different expansions.

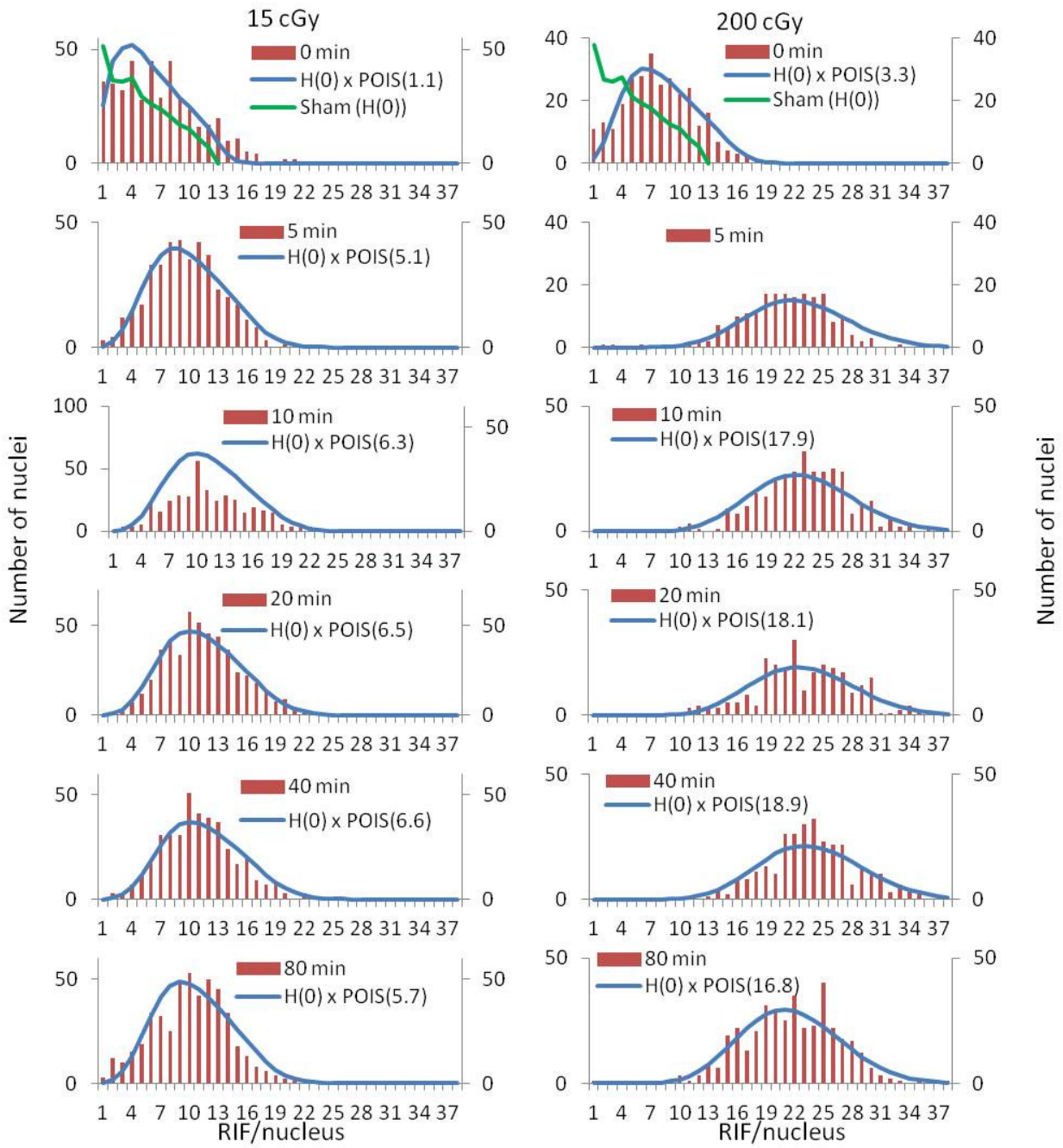

Fig. S9: Background correction. The number of RIF/nuc for each time-point following two doses (0.15 and 2 Gy) in MCF10A labeled with 53BP1 were corrected for background level of background foci. Counts distribution for RIF/nuc are shown as histogram (H(Dose)) and fitted by a Poisson distribution of mean M (POIS(M)) convolved with the foci/nuc distribution of un-irradiated specimen (green curve on top panel, H(0 Gy)). The mean M that led to the best fit, which is displayed over each histogram as a blue solid line, corresponds to the reported real RIF yield for a given time-point corrected for background foci. As one would expect, these graphs confirm that the number of real RIF/nuc follow a Poisson distribution much like the number of DSB/nuc.

DISCLAIMER

This document was prepared as an account of work sponsored by the United States Government. While this document is believed to contain correct information, neither the United States Government nor any agency thereof, nor the Regents of the University of California, nor any of their employees, makes any warranty, express or implied, or assumes any legal responsibility for the accuracy, completeness, or usefulness of any information, apparatus, product, or process disclosed, or represents that its use would not infringe privately owned rights. Reference herein to any specific commercial product, process, or service by its trade name, trademark, manufacturer, or otherwise, does not necessarily constitute or imply its endorsement, recommendation, or favoring by the United States Government or any agency thereof, or the Regents of the University of California. The views and opinions of authors expressed herein do not necessarily state or reflect those of the United States Government or any agency thereof or the Regents of the University of California.